applied sciences

MDPI

Article

In-Plane Structural Analysis of Coated Masonry Walls via a Homogenized Model

Simona Di Nino and Angelo Luongo *

Department of Civil, Construction-Architectural and Environmental Engineering, University of L'Aquila, 67100 L'Aquila, Italy; simona.dinino@univaq.it
* Correspondence: angelo.luongo@univaq.it

Abstract: An orthotropic homogenized model is used to investigate the in-plane elastic behavior of coated masonry walls. The homogenization process mainly consists of modeling the elementary cell of a three-layer medium by using suitable designed assemblies of in-parallel springs. On the basis of the latter, the stresses distributed between masonry and reinforcement coatings are analytically assessed after the determination of the average stress acting on the homogeneous medium. The precision of the theoretical outcomes is evaluated through comparisons with finite element (FE) models. Static and dynamic numerical analyses are carried out on both non-homogeneous and homogeneous FE models of sample systems. The homogeneous model is observed to adequately capture both the local and global behavior of reinforced masonry walls. Parametric analyses are also performed to investigate the effectiveness of reinforcement on the overall behavior of the system.

Keywords: coated masonry; homogenization; stress distribution; static and dynamic analyses

check for updates

Citation: Di Nino, S.; Luongo, A. In-Plane Structural Analysis of Coated Masonry Walls via a Homogenized Model. *Appl. Sci.* **2024**, *14*, 1091. https://doi.org/10.3390/app14031091

Academic Editor: José António Correia

Received: 25 November 2023
Revised: 16 December 2023
Accepted: 24 January 2024
Published: 27 January 2024

Copyright: © 2024 by the authors. Licensee MDPI, Basel, Switzerland. This article is an open access article distributed under the terms and conditions of the Creative Commons Attribution (CC BY) license (https://creativecommons.org/licenses/by/4.0/).

1. Introduction

Many masonry buildings are located in seismic areas around the world. However, the intrinsic low tensile strength of masonry makes existing structures vulnerable to seismic forces [1], and, for this reason, reinforcing interventions are often required. Some reviews about the retrofitting methods for unreinforced masonry structures can be found in [2,3]; in particular, they mention certain traditional techniques, such as methods involving surface treatments (e.g., reinforced mortar coating [4]), or to more advanced materials, such as Textile Reinforced Mortar (TRM) [5], Fiber Reinforced Polymers (FRPs) [6], and Fiber Reinforced Cementitious Matrix (FRCM) [7]. Here, the attention is mainly addressed to an alternative technique that combines the benefits of traditional methods with the utilization of advanced materials, namely the Steel Fiber Reinforced Mortar (SFRM) coating [8]. It involves the application of thin mortar coatings, reinforced with randomly distributed short fibers in the mortar matrix, either on one or both sides of masonry walls. Such a technology entails several advantages, e.g., the time-saving related to constructing thin coatings (since recommendations for minimum rebar cover are no longer necessary) and an enhanced crack control under service loading conditions (due to the improved tensile strength offered by steel fibers in the mortar). Above all, experimental tests [8–11] have proved the effectiveness of this reinforcing technique for masonry panels, especially improved performances, including increased strength and stiffness, are observed, with outcomes influenced by the steel fiber content.

In the literature, a number of researchers resort to homogenized models to investigate both unreinforced and reinforced masonry. Indeed, regarding the former, even today, macro-modeling approaches are employed, where the overall material is modeled as an equivalent homogeneous Cauchy continuum (e.g., [12–16]). The latter obeys to macroscopic constitutive laws, often derived using homogenization techniques both in elastic and non-elastic regime, e.g., [17–22]. Among these, ref. [17] is a pioneering work, which calculates

the equivalent elastic constants of unreinforced brick masonry using a two-step (horizontal and vertical) homogenization process; it is based on a straightforward mechanical system consisting of elastic springs. A similar more recent paper is [22], where a homogenization method is formulated to characterize the behavior of unreinforced masonry walls featuring a regular brick pattern. This involves employing appropriately arranged in-series and in-parallel springs to model an elementary cell and subsequently determining the "equivalent" elastic constants of a homogeneous and orthotropic material. Similarly, concerning reinforced masonry, numerous homogenization models have been developed in the literature, according to the reinforcement technology (e.g., ref. [23] relative to CFRP reinforced masonry, ref. [24] referred to FRP grids, ref. [25] for FRCM composites). However, when addressing masonry walls reinforced by SFRM coatings, there are few modeling attempts documented in the literature [8,26–29]; moreover, the only homogenization approach is proposed in the recent paper [30]. In the latter, the methods and philosophy developed in [22] for the unreinforced masonry are extended to solve a different problem, namely that of reinforced masonry. A two-step homogenization procedure (in- and out-of-wall) is employed to determine the (membrane) macroscopic elastic constants of coated masonry subjected to stress in their plane. The main result entails deriving simple closed-form expressions for the linear elastic constants of an "equivalent" homogeneous and orthotropic material.

Here, the in-plane behavior of coated masonry walls is analyzed via the homogenized model defined in [30], where only some preliminary structural analyses have been performed to prove the considerable reduction in the computational burden with respect to refined finite element models; the latter require a very dense mesh of dimension at least equal to the thickness of the thin coating. In addition, in [30] no investigation into the stress states has been carried out. On the other hand, in this paper, the stresses distributed between masonry and reinforcement elements are analytically evaluated once the average stress acting on the homogeneous medium has been determined. A systematic finite element structural analysis, under different static and dynamic load conditions, is performed to evaluate the accuracy of the simplified model in predicting both the local and global behavior of coated masonry walls, with particular attention to the stress jumps occurring at the masonry–reinforcement interfaces. Finally, the reinforcement effectiveness on the global behavior of the system is also detected in terms of modal characteristics.

The layout of the paper is as follows. In Section 2, the homogenization procedure defined in [30] is briefly described. In Section 3, the partition coefficients of the stresses between masonry and reinforcement are analytically evaluated. In the Sections 4 and 5, the accuracy of the theory is assessed through comparisons with refined finite element analyses, referred to sample systems of coated walls; moreover, parametric analyses are carried out to investigate the benefits provided by the reinforcement. Finally, in Section 6 the main findings of the work are summarized. Appendices A and B close the paper.

2. Background on the Homogenization Process

A paradigmatic model is employed to address coated masonry walls with a running/header bond pattern, as depicted in Figure 1. The masonry consists of bricks, with dimensions $a \times b \times h$, and mortar beds and joints, with a thickness c. Thin layers of SFRM, each with a thickness of t, are bonded on both sides of the masonry wall. The fundamental elements of the system, namely brick, mortar, and SFRM coatings, are considered to be homogeneous and isotropic; their elastic properties are characterized by Young modulus and Poisson ratio, denoted as (E_b, ν_b), (E_m, ν_m), and (E_s, ν_s), respectively. However, based on the assembly geometry, the resulting composite material is *non-homogeneous* and *orthotropic*.

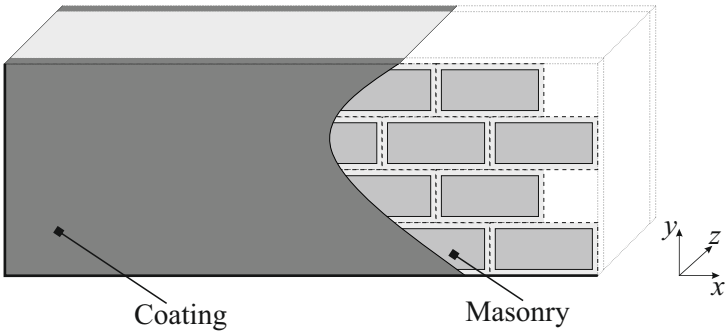

Figure 1. Coated masonry wall with regular brick pattern.

Such a system has been homogenized in [30], where it is substituted by an 'equivalent' homogeneous orthotropic material, whose constitutive law, in planar linear elasticity, is:

$$\begin{pmatrix} \varepsilon_x \\ \varepsilon_y \\ \gamma_{xy} \end{pmatrix} = \begin{bmatrix} 1/E_x & -\nu_{xy}/E_y & 0 \\ -\nu_{yx}/E_x & 1/E_y & 0 \\ 0 & 0 & 1/G_{xy} \end{bmatrix} \begin{pmatrix} \sigma_x \\ \sigma_y \\ \tau_{xy} \end{pmatrix} \tag{1}$$

In the following, to preserve the consistency of the paper, the homogenization process used in [30] to identify the equivalent five elastic constants (E_x, E_y, ν_{xy}, ν_{yx}, G_{xy}), is briefly recalled. It is denoted as (xy,z)-homogenization and consists of the following two steps:

- Step 1, xy-homogenization: it is carried out in-wall-plane (x, y) and is applied to the unreinforced masonry only;
- Step 2, z-homogenization: it is performed out-of-wall-plane (along the normal direction z) and is applied to a three-layer medium, standing for the coated wall.

It is worth mentioning that in [30], another homogenization strategy, denoted as (z,xy)-homogenization and characterized by an inverse step order, has also been developed. Such decomposition of the two processes of homogenization does not commute. This property is analogous to that found in formulating 2D homogeneous models of plates with periodic structure, namely that in-plane and transverse homogenizations do not commute (see, e.g., [31]). However, the analyses performed in [30] have shown that the two homogenization strategies yield very similar numerical results.

Below, while the homogenization performed in Step 1 is only briefly mentioned, the z-homogenization of the Step 2 is described with slightly more detail because the subsequent Section 3 is based on it.

2.1. xy-Homogenization

First, the xy-homogenization is performed by applying the strategy defined in [22] for the unreinforced wall (uw), where the elastic constants of an 'equivalent' homogeneous orthotropic material are identified by means of specific assemblies of springs, that are combined in series and/or parallel on a phenomenological basis. The following closed-form expressions are finally derived:

$$\begin{aligned} E_x^{uw} &= E_b \frac{\alpha_E(\beta_a(\beta_b+\alpha_E)+\beta_b+1)}{(\beta_a+1)(\beta_b+\alpha_E)}, \\ E_y^{uw} &= E_b \frac{\alpha_E(\beta_b(\beta_a+\alpha_E)+\beta_a+1)}{(\beta_b+1)(\beta_a+\alpha_E)}, \\ \nu_{xy}^{uw} &= \nu_b \frac{\alpha_\nu(\beta_b(\beta_a+\alpha_E)(\alpha_E\beta_a+1)+\alpha_E\beta_a(\beta_a+1))+\alpha_E(\beta_a+1)}{(\beta_b+1)(\beta_a+\alpha_E)(\alpha_E\beta_a+1)}, \\ G_{xy}^{uw} &= G_b \frac{\alpha_G(\beta_a+1)(\beta_b+1)}{\beta_a\beta_b+\beta_a+\beta_b+\alpha_G} \end{aligned} \tag{2}$$

where nondimensional quantities have been introduced:

$$\alpha_E := \frac{E_m}{E_b}, \quad \alpha_\nu := \frac{\nu_m}{\nu_b}, \quad \alpha_G := \frac{G_m}{G_b}, \quad \beta_a := \frac{c}{a}, \quad \beta_b := \frac{c}{b} \tag{3}$$

For the details of the procedure, refer to [22].

2.2. z-Homogenization

Then, the z-homogenization is performed on a three-layer medium (3LM), of dimension $A \times B$ (Figure 2a), composed of a homogeneous and orthotropic internal layer ($e = 1$), of thickness h, and of two homogeneous and isotropic external layers ($e = 2$), of thickness t. The core ($e = 1$) stands for the previously homogenized unreinforced masonry of elastic constants Equation (2), while the skins ($e = 2$) stand for the SFRM coatings of elastic constants E_s, ν_s. The 3LM is substituted with an 'equivalent' homogeneous orthotropic medium of dimensions $A \times B$ and thickness $h + 2t$ (Figure 2b), referred to as a single-layer model (1LM). The equivalent elastic constants of the latter are identified by modeling the in-plane behavior of the non-homogeneous cell by specific assemblies of in-parallel springs, as depicted in Figure 3.

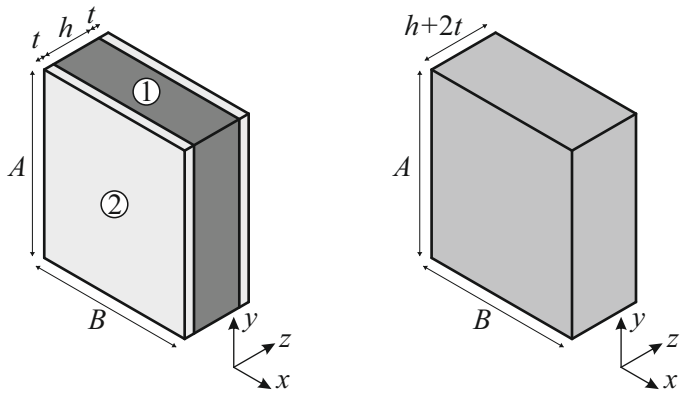

(**a**) (**b**)

Figure 2. (**a**) Non-homogeneous cell. (**b**) Homogeneous orthotropic cell. Labels 1 and 2 denote masonry and reinforcement elements.

Let us consider, for instance, the cell experiencing normal stresses, with a resultant force denoted as N_x, as depicted in Figure 3a. Elements 1 and 2 must experience identical overall elongation due to geometric considerations, specifically to maintain the rectangular shape of the cell and ensure compatibility with adjacent cells; therefore, they behave as springs working *in-parallel*, having stiffness k_{x1} and k_{x2}, respectively. Similar considerations have been made for the other in-plane behaviors. The expressions of the spring stiffness k_e ($e = 1, 2$) are reported in Appendix A.

By equalizing the total stiffness/displacement of each assembly with that of the homogeneous cell, the equivalent elastic constants are ultimately determined:

$$\begin{aligned} E_x &= E_x^{uw} \frac{(2\alpha_{Ex}\beta + 1)}{2\beta + 1}, \\ E_y &= E_y^{uw} \frac{(2\alpha_{Ey}\beta + 1)}{2\beta + 1}, \\ \nu_{xy} &= \nu_{xy}^{uw} \frac{2\alpha_{Ex}\beta\alpha_{\nu xy} + 1}{2\alpha_{Ex}\beta + 1}, \\ G_{xy} &= G_{xy}^{uw} \frac{(2\alpha_{Gxy}\beta + 1)}{2\beta + 1} \end{aligned} \tag{4}$$

where the following nondimensional parameters have been introduced:

$$\alpha_{Ex} := \frac{E_s}{E_x^{uw}}, \quad \alpha_{Ey} := \frac{E_s}{E_y^{uw}}, \quad \alpha_{\nu xy} := \frac{\nu_s}{\nu_{xy}^{uw}}, \quad \alpha_{Gxy} := \frac{G_s}{G_{xy}^{uw}}, \quad \beta := \frac{t}{h} \tag{5}$$

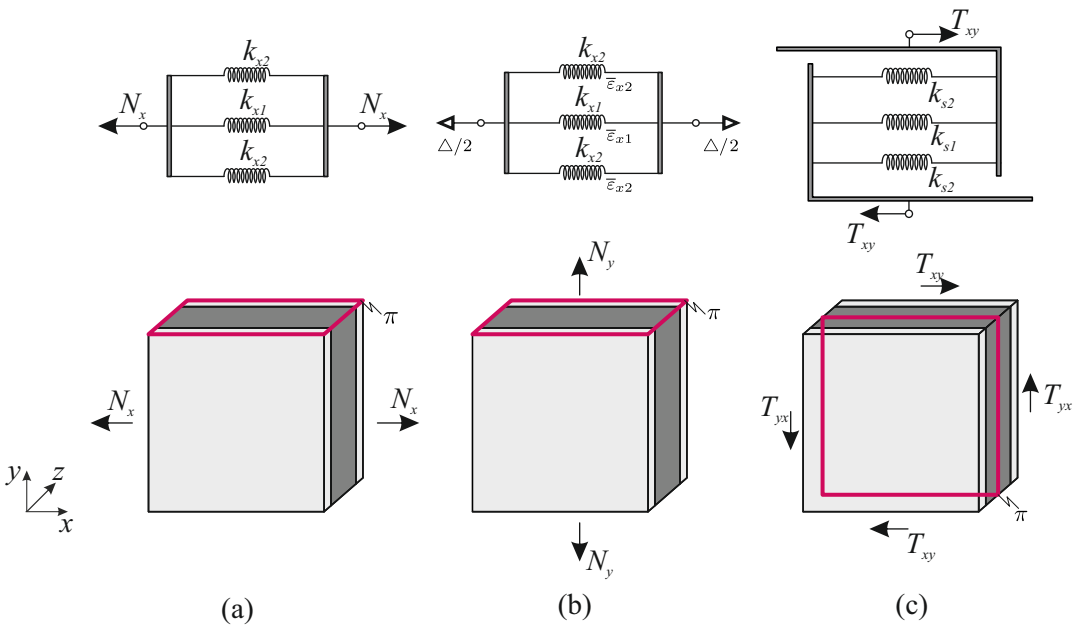

Figure 3. Spring systems for the in-plane cell behavior: (**a**) extension along x; (**b**) transverse dilatation along x; (**c**) shear.

3. Stress Distribution in the Three-Layer Model

The spring systems, defined in [30] and mentioned in Section 2.2, allow us to evaluate how the normal and shear forces, applied to the homogeneous cell (1LM), distribute themselves between the two parts 1 and 2 of the non-homogeneous cell (3LM).

3.1. Normal Stress Distribution

The *averaged* stresses of the homogeneous cell, denoted as $\bar{\sigma}_x, \bar{\sigma}_y$, involve the resulting normal forces $N_x = \bar{\sigma}_x(h+2t)A$ and $N_y = \bar{\sigma}_y(h+2t)B$, respectively.

Let us consider N_x; it distributes itself between the two parts 1 and 2 of the non-homogeneous cell, through the spring system in Figure 3a. For equilibrium $N_x = N_{x1} + 2N_{x2}$, and since the elements are in parallel, $\frac{N_{x1}}{k_{x1}} = \frac{N_{x2}}{k_{x2}}$. Therefore, by letting $\sigma_{x1} = \frac{N_{x1}}{h}$ and $\sigma_{x2} = \frac{N_{x2}}{t}$, it follows:

$$\begin{aligned} \sigma_{x1} &= \frac{2\beta+1}{1+2\alpha_{Ex}\beta}\bar{\sigma}_x, \\ \sigma_{x2} &= \frac{\alpha_{Ex}(2\beta+1)}{1+2\alpha_{Ex}\beta}\bar{\sigma}_x \end{aligned} \tag{6}$$

where the definitions (5) have been used.

In the same way:

$$\begin{aligned} \sigma_{y1} &= \frac{2\beta+1}{1+2\alpha_{Ey}\beta}\bar{\sigma}_y, \\ \sigma_{y2} &= \frac{\alpha_{Ey}(2\beta+1)}{1+2\alpha_{Ey}\beta}\bar{\sigma}_y \end{aligned} \tag{7}$$

These expressions enable the assessment of (local) stress within the components of the non-homogeneous medium (specifically in the masonry and reinforcement), starting from

the average normal stress acting on the homogenized medium ($\bar{\sigma}_x$ or $\bar{\sigma}_y$). Furthermore, for small values of β, the preceding local stress expressions can be approximated as:

$$\begin{aligned} \sigma_{x1} &\simeq \bar{\sigma}_x, \\ \sigma_{x2} &\simeq \alpha_{Ex}\bar{\sigma}_x \end{aligned} \tag{8}$$

$$\begin{aligned} \sigma_{y1} &\simeq \bar{\sigma}_y, \\ \sigma_{y2} &\simeq \alpha_{Ey}\bar{\sigma}_y \end{aligned} \tag{9}$$

It means that the masonry normal stress is about equal to the global stress of the homogenized model, while the reinforcement normal stress is proportional to the former via the reinforced-to-unreinforced masonry modulus ratio α_{Ex} or α_{Ey}.

3.2. Self-Stress State

Also in this case, an interesting investigation concerns the distribution of the self-stress state $\tilde{\sigma}_{xe}, \tilde{\sigma}_{ye}$, resulting from the transverse-to-load behavior of the non-homogeneous cell under the normal forces N_y and N_x, respectively.

Let us consider the transverse dilatation along x (due to N_y), modeled by the spring system in Figure 3b, where $\triangle/2$ is the unknown displacement at nodes. By denoting with F_{xe} the elastic force at the spring e, the elastic problem is governed by:

$$\begin{aligned} F_{x1} &= k_{x1}(\triangle - \bar{\varepsilon}_{x1}B), \\ F_{x2} &= k_{x2}(\triangle - \bar{\varepsilon}_{x2}B) \end{aligned} \tag{10}$$

which express the elastic law for the springs, and by:

$$F_{x1} + 2F_{x2} = 0 \tag{11}$$

which expresses the equilibrium condition at the nodes. The resolution to this problem, specifically, the overall elongation of the assembly, is as follows:

$$\Delta = -\frac{(2\beta+1)(\alpha_{Ex}+2\beta\alpha_{\nu xy})}{(2\beta+\alpha_{Ex})(2\beta\alpha_{Ey}+1)}\frac{\nu_{xy}^{uw}}{E_y^{uw}}B\bar{\sigma}_y \tag{12}$$

By substituting the solution Equation (12) in Equation (10), the spring forces are evaluated and, by letting $\tilde{\sigma}_{x1} = \dfrac{F_{x1}}{hA}$, $\tilde{\sigma}_{x2} = \dfrac{F_{x2}}{tA}$, it follows:

$$\begin{aligned} \tilde{\sigma}_{x1} &= \frac{2\beta\alpha_{Ex}(2\beta+1)(1-\alpha_{\nu xy})}{(2\alpha_{Ex}\beta+1)(2\alpha_{Ey}\beta+1)}\nu_{xy}^{uw}\frac{E_x^{uw}}{E_y^{uw}}\bar{\sigma}_y, \\ \tilde{\sigma}_{x2} &= \frac{\alpha_{Ex}(2\beta+1)(-1+\alpha_{\nu xy})}{(2\alpha_{Ex}\beta+1)(2\alpha_{Ey}\beta+1)}\nu_{xy}^{uw}\frac{E_x^{uw}}{E_y^{uw}}\bar{\sigma}_y \end{aligned} \tag{13}$$

In the same way:

$$\begin{aligned} \tilde{\sigma}_{y1} &= \frac{2\alpha_{Ey}\beta(2\beta+1)(1-\alpha_{\nu yx})}{(2\alpha_{Ey}\beta+1)(2\alpha_{Ex}\beta+1)}\nu_{xy}^{uw}\bar{\sigma}_x, \\ \tilde{\sigma}_{y2} &= \frac{\alpha_{Ey}(2\beta+1)(-1+\alpha_{\nu yx})}{(2\alpha_{Ey}\beta+1)(2\alpha_{Ex}\beta+1)}\nu_{xy}^{uw}\bar{\sigma}_x \end{aligned} \tag{14}$$

with the nondimensional coefficient $\alpha_{\nu yx} = \alpha_{\nu xy}\dfrac{E_y^{uw}}{E_x^{uw}}$.

It should be noticed that, from Equation (13), $\dfrac{\tilde{\sigma}_{x2}}{\tilde{\sigma}_{x1}} = -\dfrac{1}{2\beta}$ follows; since β is small (because the wall is much thicker than the reinforcing coating), it turns out that $\tilde{\sigma}_{x1} \ll \tilde{\sigma}_{x2}$, that is, the self-stress at the masonry is negligible. Conversely, the self-stress at the

reinforcement can be significant. Similar considerations arise from Equation (14). Thus, for small values of β, the self-stress expressions can be approximated as:

$$\begin{aligned} &\tilde{\sigma}_{x1} \simeq 0, \\ &\tilde{\sigma}_{x2} \simeq \alpha_{Ex}(1-\alpha_{\nu xy})\nu_{xy}^{uw}\frac{E_x^{uw}}{E_y^{uw}}\bar{\sigma}_y \end{aligned} \tag{15}$$

and

$$\begin{aligned} &\tilde{\sigma}_{y1} \simeq 0, \\ &\tilde{\sigma}_{y2} \simeq \alpha_{Ey}(1-\alpha_{\nu yx})\nu_{xy}^{uw}\bar{\sigma}_x \end{aligned} \tag{16}$$

Finally, the total stress is determined by the combination of self-stress induced by transverse elongation and the stress triggered by axial elongation:

$$\begin{aligned} \hat{\sigma}_{xe} &= \sigma_{xe} + \tilde{\sigma}_{xe}, \\ \hat{\sigma}_{ye} &= \sigma_{ye} + \tilde{\sigma}_{ye} \end{aligned} \tag{17}$$

for $e = 1, 2$ and where Equations (6), (7), (13) and (14) hold.

3.3. Shear Stress Distribution

By denoting by $\bar{\tau}_{xy}$ the *averaged* shear stress of the homogeneous cell, the resulting horizontal and vertical shear forces are $T_{xy} = \bar{\tau}_{xy}(h+2t)B$ and $T_{yx} = \bar{\tau}_{xy}(h+2t)A$, respectively.

Let us consider the spring system in Figure 3c to evaluate how they distribute themselves between the elements 1 and 2 of the non-homogeneous cell. For equilibrium $T_{xy} = T_{xy1} + 2\,T_{xy2}$, and since the elements are in parallel, $\frac{T_{xy1}}{k_{s1}} = \frac{T_{xy2}}{k_{s2}}$. Therefore, by letting $\tau_{xy1} = \frac{T_{xy1}}{hB}$ and $\tau_{xy2} = \frac{T_{xy2}}{tB}$, it follows:

$$\begin{aligned} \tau_{xy1} &= \frac{2\beta+1}{1+2\alpha_G\beta}\bar{\tau}_{xy}, \\ \tau_{xy2} &= \frac{\alpha_G(2\beta+1)}{1+2\alpha_G\beta}\bar{\tau}_{xy} \end{aligned} \tag{18}$$

where the definitions (5) have been used. These expressions allow us to evaluate the (local) shear stress in the constituents of the non-homogeneous medium, starting from the average shear stress acting in the homogenized medium ($\bar{\tau}_{xy}$). Moreover, for small values of β, Equation (18) can be approximated by:

$$\begin{aligned} \tau_{xy1} &\simeq \bar{\tau}_{xy}, \\ \tau_{xy2} &\simeq \alpha_G\bar{\tau}_{xy} \end{aligned} \tag{19}$$

4. Static Structural Analysis and Model Validation

Static structural analyses, under different static load conditions, are carried out to investigate the accuracy of the homogenized model in describing both the local and global in-plane behavior of coated masonry walls.

4.1. Sample Systems and FE Models

Two sample systems, denoted as Sample System 1 (without openings) and Sample System 2 (with a central opening), whose in-plane geometry is represented in Figure 5, are studied here: $H = 2$ m and $L = 3$ m. The elastic and geometric characteristics of the basic components of both systems, i.e., brick, mortar, and SFRM coating, are described in Table 1, together with the mass densities of each of them (i.e., ρ_b, ρ_m, ρ_s respectively).

Table 1. Elastic, geometric, mass characteristics of brick, mortar, and SFRM coating.

Brick	$E_b = 9$ GPa, $\nu_b = 0.15$ $a = 19$ cm, $b = 25$ cm, $h = 30$ cm $\rho_b = 850$ kg/m^3
Mortar	$E_m = 4$ GPa, $\nu_m = 0.2$ $c = 1$ cm $\rho_m = 1400$ kg/m^3
SFRM Coating	$E_s = 25$ GPa, $\nu_s = 0.18$ $t = 2.5$ cm $\rho_s = 1800$ kg/m^3

Accordingly, the results of the homogenization steps are presented in Table 2.

Table 2. Numerical outcomes of the (xy,z)-homogenization.

Step 1: xy-Homogenization (Equation (2))	**Step 2: z-Homogenization (Equation (4))**
$E_x^{uw} = 8.358$ GPa $E_y^{uw} = 8.299$ GPa $\nu_{xy}^{uw} = 0.1496$ $G_{xy}^{uw} = 3.504$ GPa	$E_x = 10.735$ GPa $E_y = 10.685$ GPa $\nu_{xy} = 0.15974$ $G_{xy} = 4.5170$ GPa

Three FE models are implemented for each sample system (see, for example, the representation in Figure 4 for Sample System 1):

- 3LM: a *non-homogeneous* three-layer model, denoted as "fine model", composed of three Cauchy continuum bodies, defined in a 3D space (x, y, z) (Figure 4a). The internal medium stands for the homogenized unreinforced masonry, and, therefore, it obeys to a hyperelastic orthotropic linear law whose in-plane constitutive parameters are reported in Table 2-step 1. Its equivalent mass density is derived by simple average operations on volume, from which $\rho^{uw} = 897.596$ kg/m^3. The two external layers stand for the SFRM coatings, modeled as isotropic and homogeneous medium whose characteristics are in Table 1. The out-of-plane elastic moduli are assumed to be equal to those in-plane, while the out-of-plane Poisson ratios are set to zero. Quadratic serendipity tetrahedral finite elements are used. Adherence conditions are assured at the each element boundary. The model has 239,251 elements and 1,040,793 d.o.f. (the mesh pattern is shown in Figure A1a).
- 1LM-3D: a *homogeneous* one-layer model, consisting of one Cauchy continuum body defined in a 3D space (x, y, z) (Figure 4b). It stands for the reinforced masonry, previously homogenized, obeying to a hyperelastic orthotropic linear law whose in-plane constitutive parameters are described in Table 2-step 2. The equivalent mass density is determined through straightforward averaging operations on volume, from which $\rho = 1026.51$ kg/m^3. The out-of-plane elastic moduli and Poisson factors are assumed to be equal to those in-plane and zero, respectively. Quadratic serendipity tetrahedral finite elements are used. The model has 27,859 elements and 122,355 d.o.f. (the mesh pattern is shown in Figure A1b).
- 1LM-2D: a *homogeneous* one-layer model, consisting of one shell element behaving as a Cauchy continuum in plane stress. Also this model stands for the homogenized reinforced masonry, and, therefore it has the same elastic and mass characteristics of the 1LM-3D. The model has 1800 rectangular elements and 5490 d.o.f. (the mesh pattern is shown in Figure A1c).

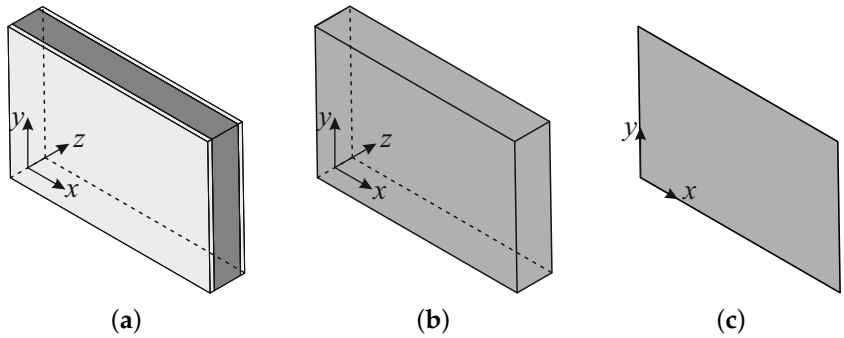

Figure 4. FE models of Sample System 1: (**a**) 3LM; (**b**) 1LM-3D; (**c**) 1LM-2D.

The numerical FE analyses are performed for both case studies by means of commercial software and using a linear solver; the walls are constrained at the bottom side and free at the remaining three sides. The calculation times are 236 s, 16 s, and 1 s for 3LM, 1LM-3D, and 1LM-2D, respectively.

4.2. Results

Static analyses are performed for the sample systems described earlier, considering two typical load conditions illustrated in Figure 5: (a) a uniform distribution of horizontal forces is applied along the left vertical side of the Sample System 1; (b) a uniform distribution of vertical forces is applied along a portion ($\frac{L}{3}$) of the top side of the Sample System 2. The magnitude of load for unit of area is taken $p_0 = 100$ kPa.

In Figure 5, the contour plots of the resultant displacements on the deformed configurations are also illustrated. Other numerical results are shown ahead, in terms of displacement and stress. The used unit of measurement for displacements, space coordinates, and stresses are cm, m, and kPa, respectively.

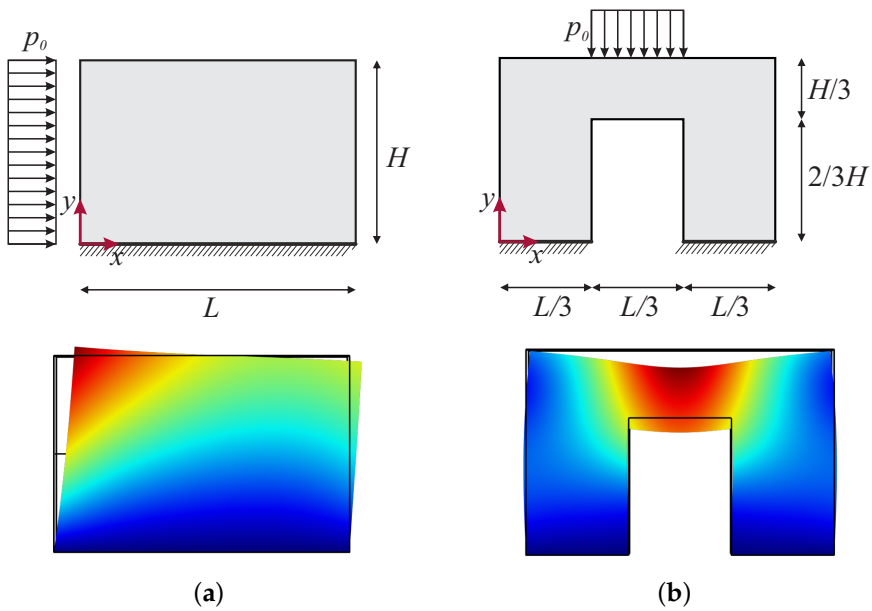

Figure 5. Load case schemes and qualitative contour plots of the displacement magnitude on deformed configuration, at the middle plane ($z = 0$), of: (**a**) Sample System 1; (**b**) Sample System 2. The displacements range from a maximum of about 0.004 cm (red color) to a minimum of 0 cm (blue color).

4.2.1. Sample System 1

Results relevant to 3LM and 1LM-3D of the Sample System 1 are reported first.

The curves in Figure 6a,b show a comparison in terms of displacements, evaluated at the sections $x = \dfrac{L}{2}$ and $y = \dfrac{H}{2}$, respectively, of the middle plane of the wall ($z = 0$); a very strong agreement is observed as the curves overlap.

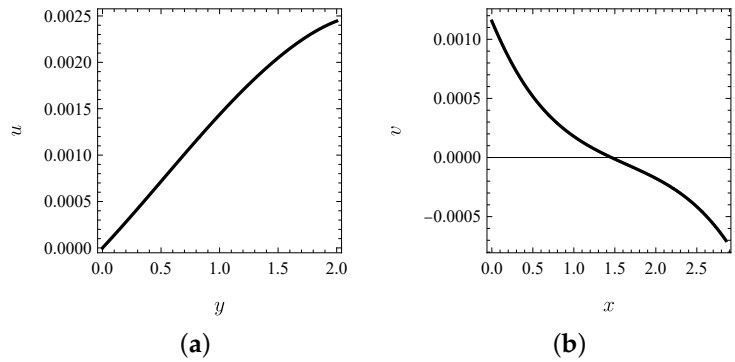

Figure 6. Displacement curves at the middle plane of the panel: (**a**) $u\left(\frac{L}{2}, y\right)$; (**b**) $v\left(x, \frac{H}{2}\right)$. 3LM (gray line) and 1LM-3D (black line).

In Figure 7, normal and shear stresses in the 3LM (gray lines) and 1LM-3D (black lines), along given selected lines, are shown: the curves (-a, -b, -c) refer at the vertical section $x = \dfrac{L}{2}$ of the middle plane of each element, while the curves (-d, -e, -f) refer to variations along the thickness z at the section $x = \dfrac{L}{2}$ of the base wall. It is seen that the results obtained by the homogeneous model fit *on average* those of the non-homogeneous model, since the true stress distribution fast changes in passing through internal and external layers.

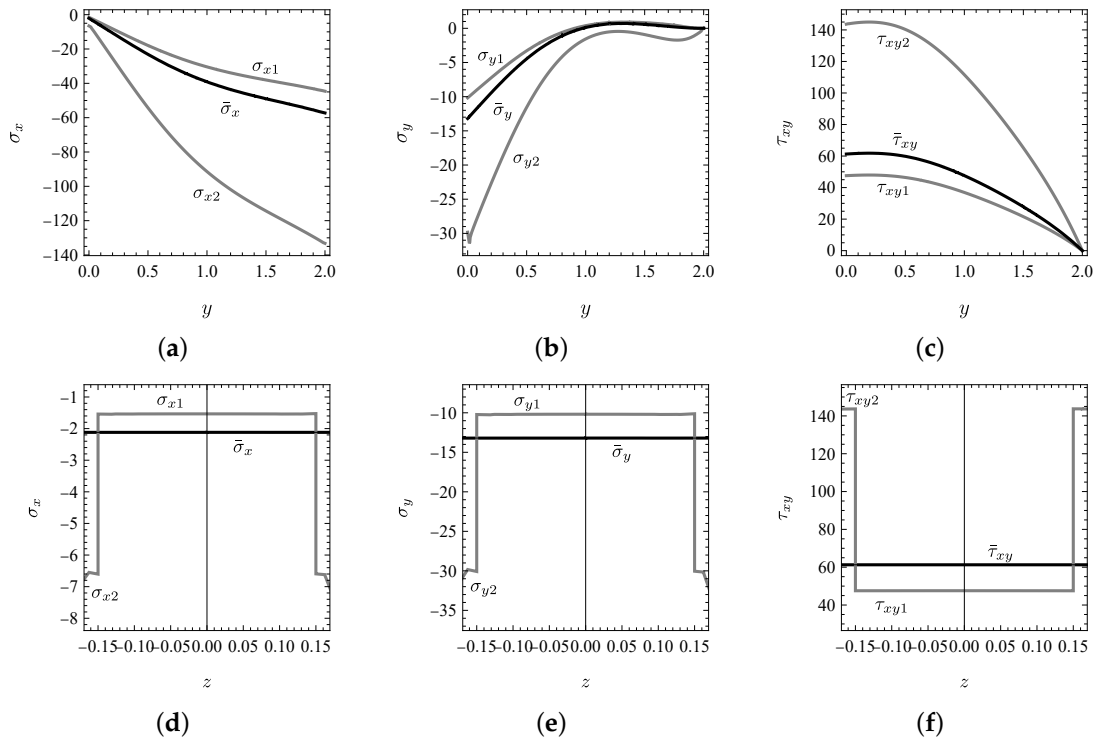

Figure 7. Stress curves: (**a**) $\sigma_x\left(\frac{L}{2}, y\right)$, (**b**) $\sigma_y\left(\frac{L}{2}, y\right)$, and (**c**) $\tau_{xy}\left(\frac{L}{2}, y\right)$ at the middle plane of each element and (**d**) $\sigma_x\left(\frac{L}{2}, z\right)$, (**e**) $\sigma_y\left(\frac{L}{2}, z\right)$, and (**f**) $\tau_{xy}\left(\frac{L}{2}, z\right)$ at the wall base. 3LM (gray line) and 1LM-3D (black line).

Then, the stresses soliciting the (homogenized) masonry and the reinforcement, as furnished by the analytical model (Equations (17) and (18)) starting from 1LM-3D, are shown in Figure 8 (red lines). Remarkably, the analytical predictions approximate the stress distributions detected from the 3LM (gray lines) to a very satisfactory extent, despite the fact that the homogeneous model is aimed at describing global, and not local, behavior. However, upon closer inspection of Figure 8b, a slight deviation is observed between red and gray curves near the free end ($y = H$), where the stresses of the 3LM (gray lines) cancel out, while those resulting from the analytical distribution (red lines) are nonzero, although with zero average. Such a phenomenon is related to the existence of boundary layers (e.g., [32]), where it is known that the homogenization is satisfactory far away from the free edges. In order to further investigate this issue, normal and shear stresses acting along the horizontal section $y = \dfrac{H}{2}$ are also determined in Figure 9. It is seen that the 3LM exhibits a boundary layer near the loaded edge ($x = 0$), which the homogeneous model (1LM) fails to capture.

In addition, the effect of the self-stresses is highlighted in Figure 10, where the laws $\sigma_x\left(\frac{L}{2}, y\right)$ and $\sigma_y\left(\frac{L}{2}, y\right)$, excluding (dashed lines) and including (solid lines) the self-stresses, are plotted in a small y-range. It appears that self-stress is negligible at the homogenized masonry (the curves are quasi superimposed), while it is significant at the reinforcement layers.

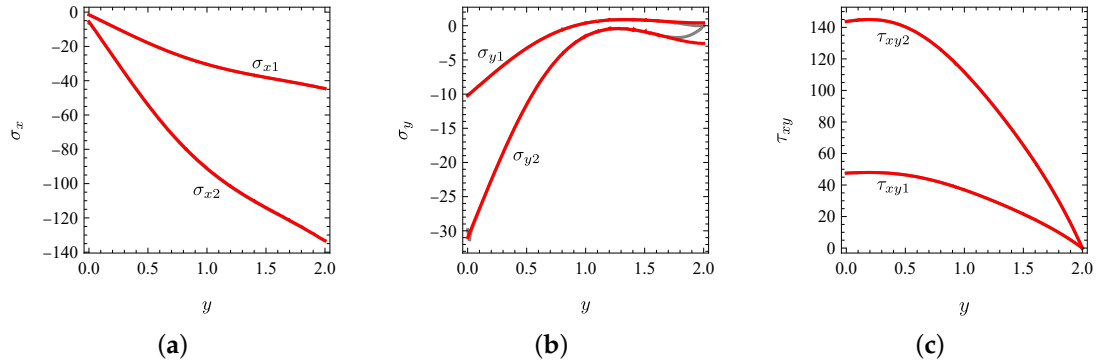

(**a**) (**b**) (**c**)

Figure 8. Stress curves: (**a**) $\sigma_x\left(\frac{L}{2}, y\right)$; (**b**) $\sigma_y\left(\frac{L}{2}, y\right)$, and (**c**) $\tau_{xy}\left(\frac{L}{2}, y\right)$. 1LM-3D (red lines) vs. 3LM (gray lines) distributions.

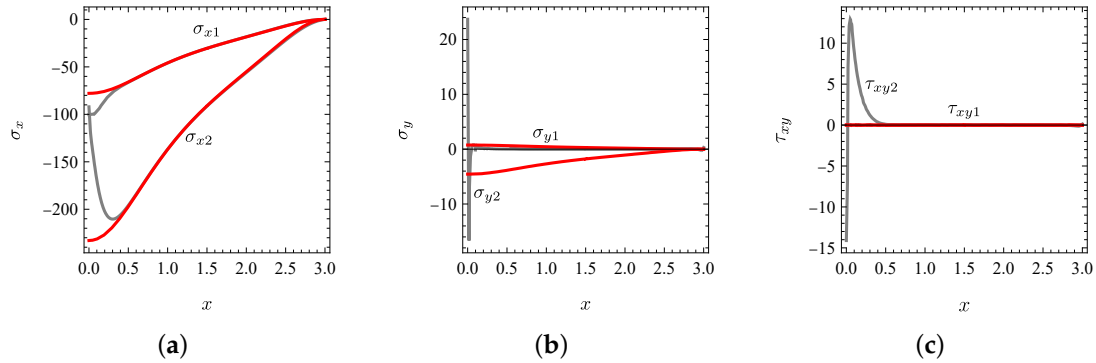

(**a**) (**b**) (**c**)

Figure 9. Stress curves: (**a**) $\sigma_x\left(x, \frac{H}{2}\right)$; (**b**) $\sigma_y\left(x, \frac{H}{2}\right)$, and (**c**) $\tau_{xy}\left(x, \frac{H}{2}\right)$. 1LM-3D (red lines) vs. 3LM (gray lines) distributions.

Finally, a comparison between 1LM-3D and 1LM-2D is also made in terms of displacement and global stress in Figure 11. The coarse shell model (i.e., 1LM-2D), is observed to approximate the results of 1LM-3D very effectively, despite having a reduced number of degrees of freedom.

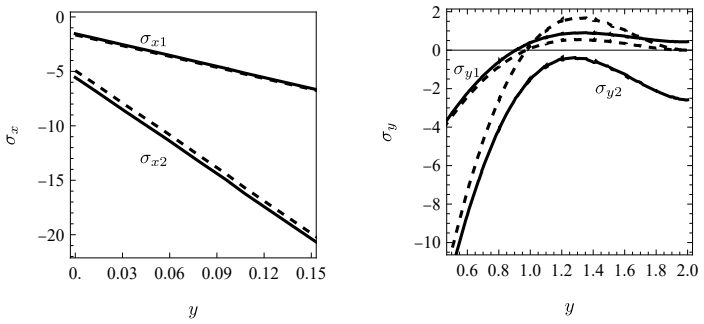

(**a**) (**b**)

Figure 10. Normal stress curves derived by 1LM-3D: (**a**) $\sigma_x\left(\frac{L}{2}, y\right)$; (**b**) $\sigma_y\left(\frac{L}{2}, y\right)$; zoom on a small y-range. Distribution between homogenized masonry and reinforcement, excluding (dashed lines) and including (solid lines) the self-stresses.

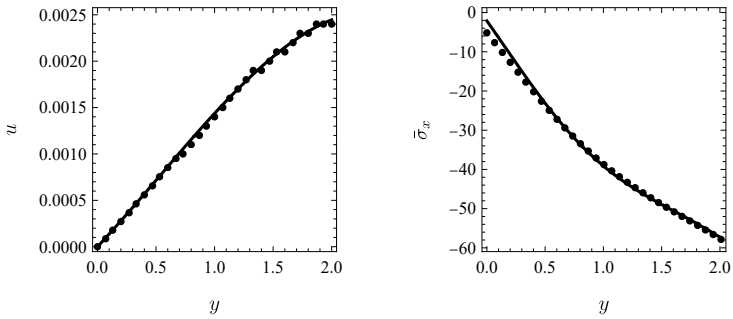

(**a**) (**b**)

Figure 11. Comparison between 1LM-3D and 1LM-2D: (**a**) $u\left(\frac{L}{2}, y\right)$; (**b**) $\bar{\sigma}_x\left(\frac{L}{2}, y\right)$. 1LM-3D (black solid line) and 1LM-2D (black dots).

4.2.2. Sample System 2

Results relevant to 3LM and 1LM-3D of the Sample System 2 are reported.

A first comparison in terms of displacement is shown in Figure 12, along the horizontal section $y = H$ of the middle plane of the wall; it is seen that the curves are almost coincident.

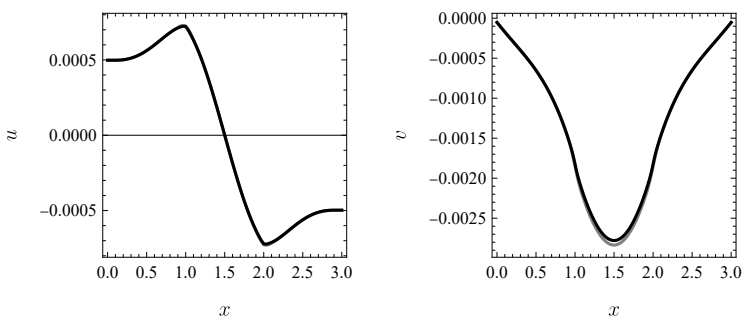

(**a**) (**b**)

Figure 12. Displacement curves at the middle plane of the wall: (**a**) $u(x, H)$; (**b**) $v(x, H)$. 3LM (gray line) and 1LM-3D (black line).

A sketch of the stress distribution in the domain of 3LM is provided by the contour plots of the minimum and maximum principal stresses, shown in Figure 13a,b, respectively; in addition, in Figure 13c, four measuring points, having in-plane coordinates A $= \left(\frac{L}{2}, \frac{5H}{6}\right)$, B $= \left(\frac{L}{3}, \frac{5H}{6}\right)$, C $= \left(\frac{L}{6}, \frac{2H}{3}\right)$, and D $= \left(\frac{L}{6}, \frac{H}{3}\right)$, are illustrated. Just in these points, the normal and shear stresses soliciting the internal and external layers of the 3LM, evaluated

at the middle plane of each element, are compared with those furnished by the analytical model (according to Equations (17) and (18)) starting from 1LM-3D; the percentage errors are reported in Table 3. Once again, the accuracy of the homogeneous model is confirmed.

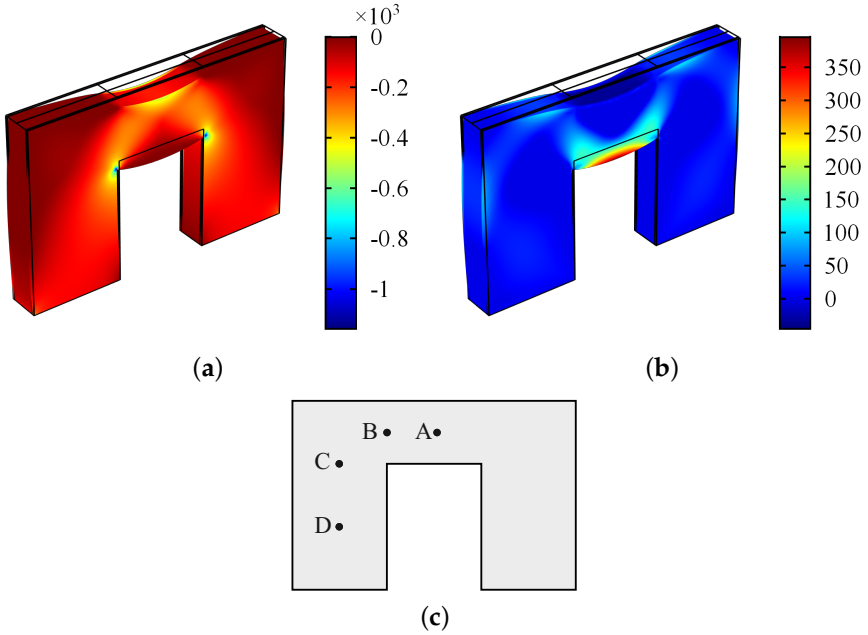

Figure 13. Contour plots of (**a**) minimum and (**b**) maximum principal stresses of 3LM. (**c**) In-plane representation of four measuring points A, B, C, and D.

Table 3. Comparison between 1LM-3D and 3LM stress distributions, evaluated in the points A, B, C, and D: percentage errors.

		σ_{xe}	σ_{ye}	τ_{xye}
A	$e = 1$	−1.76%	−6.36%	-
	$e = 2$	0.42%	3.63%	-
B	$e = 1$	−1.14%	−2.39%	−1.36%
	$e = 2$	1.81%	1.06%	0.0888%
C	$e = 1$	−0.0176%	0.355%	0.134%
	$e = 2$	−0.642%	−0.239%	0.0209%
D	$e = 1$	2.26%	0.168%	−0.265%
	$e = 2$	−1.34%	−0.362%	−0.0891%

5. Modal Dynamic Analysis

The natural frequencies provide a "global" measure of the performance, in elastic regime, of a structural system. Therefore, modal dynamic analyses are carried out to: (i) further asses the (global) agreement between non-homogeneous and homogeneous models of the previous sample systems; (ii) evaluate the effectiveness of the reinforcement, through parametric studies.

5.1. Benchmark Results

Results relevant to 3LM, 1LM-3D, and 1LM-2D of both sample systems described in Section 4.1 are reported. They consist of the frequencies f_i ($i = 1, 2, 3$) of the first three natural vibration modes, in Table 4, together with the corresponding modal shapes, in Figure 14. It is observed that the homogenized model well approximates the in-plane behavior of this kind of systems, with a very small percentage error.

Table 4. Comparison between natural frequencies (in [Hz]) of homogeneous vs. non-homogeneous models: (a) Sample System 1; (b) Sample System 2. Percentage error in brackets.

Modal Frequency	3LM	1LM-3D	1LM-2D
		(a)	
f_1	200.96	200.95 (−0.0050%)	201.085 (0.062%)
f_2	403.81	403.77 (−0.0099%)	403.75 (−0.015%)
f_3	449.67	449.69 (0.0044%)	449.90 (0.051%)
		(b)	
f_1	129.22	129.21 (−0.0077%)	130.259 (0.80%)
f_2	314.32	314.31 (−0.0032%)	315.677 (0.43%)
f_3	397.99	397.97 (−0.0050%)	397.881 (−0.027%)

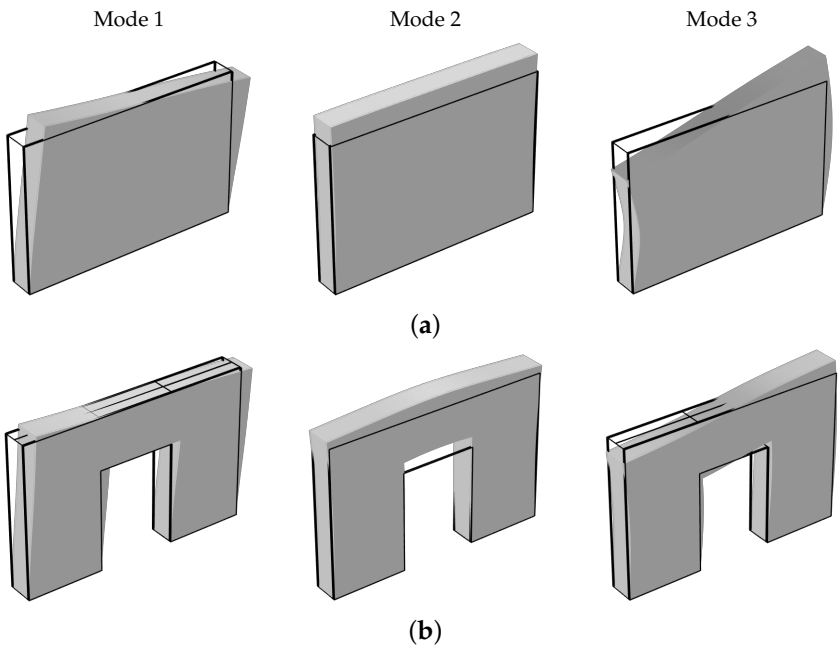

Figure 14. Modal shapes: (**a**) Sample System 1; (**b**) Sample System 2.

5.2. Parametric Analysis

Parametric analyses are numerically performed on the fine model (3LM) of the Sample System 1 only to examine the influence of both SFRM modulus and coating thickness (through the ratios α_{Ex} and β of Equation (5)) on the natural frequencies f_i ($i = 1, 2, 3$). The latter, compared to those of the unreinforced wall f_i^{uw}, are displayed in Figures 15 and 16. It is observed that, within the ranges examined, the natural frequencies can be increased by up to 45%, in relation to the elastic modulus of the reinforcement (see Figure 15); on the contrary, the coating thickness has little influence on the system dynamics, producing a frequency increment of up to 8% (see Figure 16). In addition, it is worth noting that the reinforcement affects the different vibration modes at the same way.

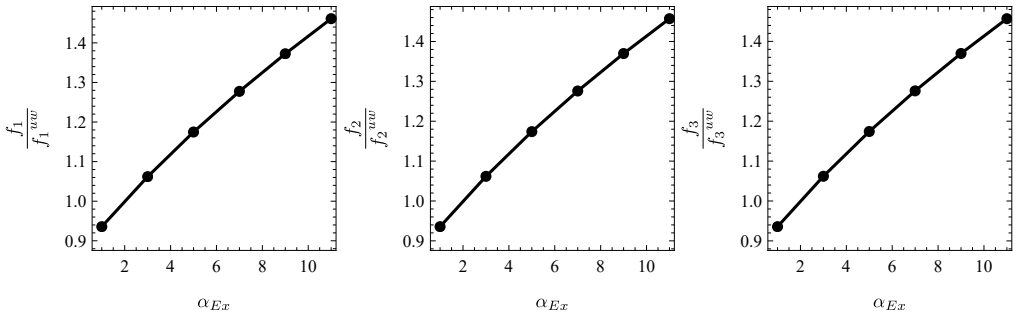

Figure 15. Natural frequencies of the non-homogeneous model vs. reinforced-to-unreinforced wall modulus ratio, for the Sample System 1; numerical results (black dots) and interpolating laws (solid black lines).

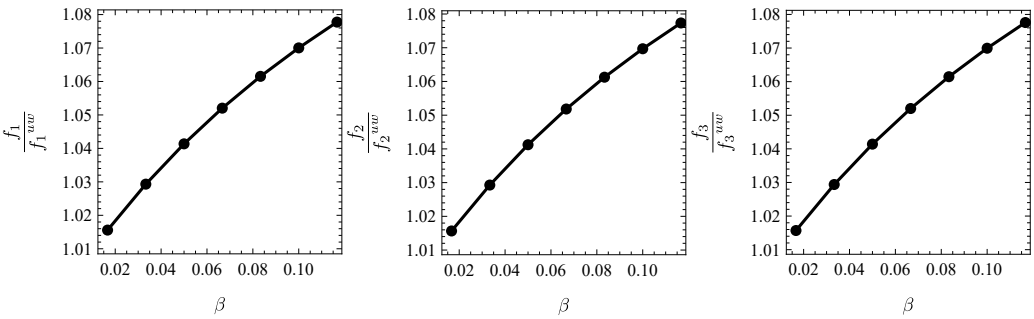

Figure 16. Natural frequencies of the non-homogeneous model vs. coating-to-wall thickness ratio, for the Sample System 1; numerical results (black dots) and interpolating laws (solid black lines).

6. Conclusions

The in-plane behavior of coated masonry walls has been analyzed via a homogenized orthotropic model, based on suitable designed assemblies of in-parallel springs. Accordingly, the stresses distributed between masonry and reinforcement coatings have been evaluated analytically, once the average stress acting on the homogeneous medium has been determined. Static and dynamic numerical analyses have been carried out on both non-homogeneous and homogeneous FE models of two sample systems. Parametric analyses have been also performed to investigate the reinforcement influence on the global behavior of the system.

The following main conclusions are drawn:

- Homogenized FE models of coated wall systems enable structural analysis to be performed with a significantly reduced computational burden. This is especially true when much coarser 2D homogeneous models are used, while still achieving excellent results. This outcome, which was recently discovered in [30] based on a few preliminary structural analyses on scale models, has been corroborated here. For instance, concerning Sample System 1, the calculation time of the refined model (3LM) is found to be 236 times greater than that of the homogenized one (1LM-2D).
- The homogeneous model is able to accurately describe the local displacement field of the non-homogeneous model, while it fits *on average* the stress fields, due to the fast changes occurring across the constituent boundaries. However, when the average stress is partitioned between masonry and reinforcement via closed-form formulae, the stress peaks in each element are captured, in spite of the fact the homogeneous model is aimed at describing global, and not local, behavior. The effect of a self-stress state in the elements, triggered by the Poisson effect, is also considered. It has been found to be significant mainly at the reinforcement layers. These results are of particular importance in structural field, since: (i) local analyses are aimed at strength verification of each component (i.e., masonry and reinforcement), to asses the effectiveness of SFRM application; (ii) global analyses, on the other hand, allow for estimating how the reinforcement modifies the overall mechanical behavior.

- As evidenced by parametric analyses (within the explored range of parameters), it has been observed that increasing the elastic moduli or the thickness of the reinforcement results in an increase in the natural frequencies of a given structural system, due to the application of reinforcement. This increase can be up to approximately 50%, depending on the elastic moduli of the reinforcement. On the other hand, the thickness of the coating has a less significant impact on the system dynamics, as it leads to frequency increments of up to 10%.

A future prospect of the work could involve performing experimental tests and more extensive numerical simulations to enhance confidence in analytical predictions and highlight the advantages of homogenization. For instance, this could include estimating the reduction in calculation time for a real-size building.

Author Contributions: Conceptualization, A.L.; Methodology, S.D.N. and A.L.; Software, S.D.N.; Validation, S.D.N.; Formal analysis, S.D.N.; Writing—original draft, S.D.N.; Writing—review & editing, S.D.N. and A.L.; Supervision, A.L. All authors have read and agreed to the published version of the manuscript.

Funding: This research received no external funding.

Data Availability Statement: Data are contained within the article.

Conflicts of Interest: The authors declare no conflict of interest.

Appendix A. Equivalent Springs

It is known that a plate under an uniform strain state (such as extension along the x or y or shear) behaves like an equivalent elastic spring whose stiffness needs to be identified. This has been made in [30] by equating the elastic energy of the plate to that of the spring. Below, the expressions of the equivalent stiffness of each spring in Figure 3 are reported:

- For the extension and transverse dilatation along x (Figure 3a,b):

$$k_{x1} = \frac{A}{B} h E_x^{uw}, \qquad k_{x2} = \frac{A}{B} t E_s \tag{A1}$$

- For the shear (Figure 3c):

$$k_{s1} = G_{xy}^{uw} h \frac{B}{A}, \qquad k_{s2} = G_s t \frac{B}{A} \tag{A2}$$

Moreover, in the horizontal dilatation in Figure 3b, each spring of the assembly undergoes a prescribed dilation, $\bar{\varepsilon}_{xe}$, due to the Poisson effect, i.e., proportional to the vertical stress of the corresponding element, σ_{ye}, namely:

$$\bar{\varepsilon}_{x1} = -\frac{\nu_{xy}^{uw}}{E_y^{uw}} \sigma_{y1}, \qquad \bar{\varepsilon}_{x2} = -\frac{\nu_s}{E_s} \sigma_{y2} \tag{A3}$$

Appendix B. Mesh Pattern Representations

With reference to the Sample System 1, the used mesh pattern is shown in Figure A1, for 3LM, 1LM-3D, and 1LM-2D, respectively.

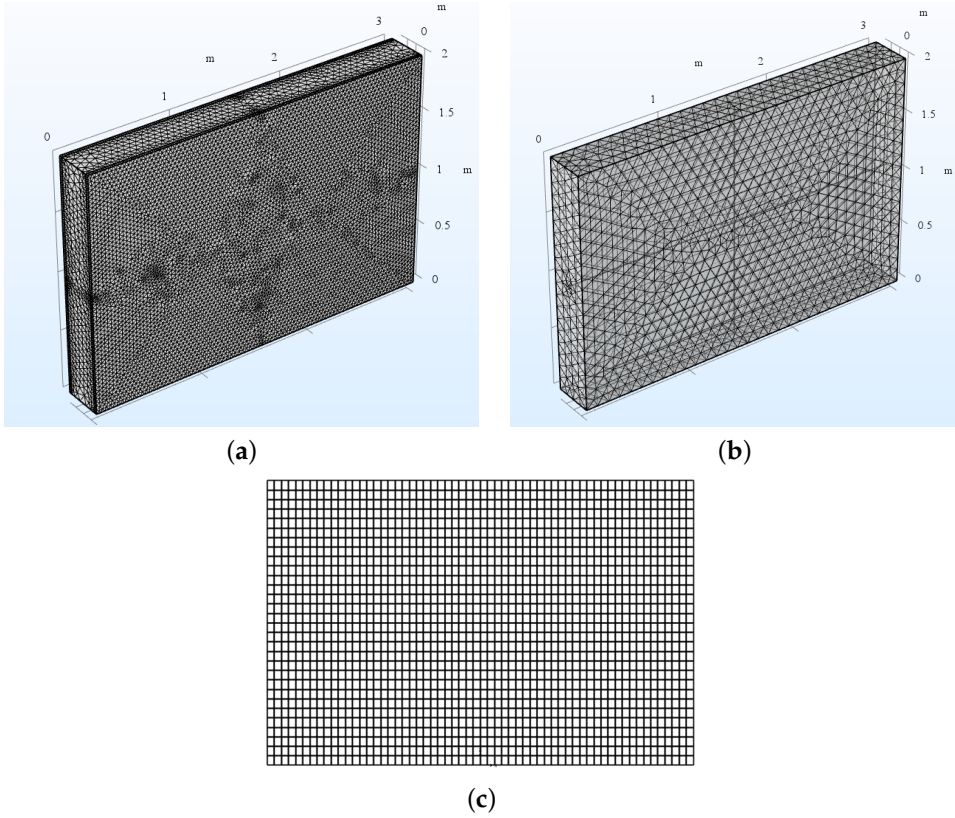

Figure A1. Mesh pattern in: (**a**) 3LM, (**b**) 1LM-3D, and (**c**) 1LM-2D of the Sample System 1.

References

1. D'Ayala, D.; Speranza, E. Definition of collapse mechanisms and seismic vulnerability of historic masonry buildings. *Earthq. Spectra* **2003**, *19*, 479–509. [CrossRef]
2. Bhattacharya, S.; Nayak, S.; Dutta, S.C. A critical review of retrofitting methods for unreinforced masonry structures. *Int. J. Disaster Risk Reduct.* **2014**, *7*, 51–67. [CrossRef]
3. Yavartanoo, F.; Kang, T.H.K. Retrofitting of unreinforced masonry structures and considerations for heritage-sensitive constructions. *J. Build. Eng.* **2022**, *49*, 103993. [CrossRef]
4. Messali, F.; Metelli, G.; Plizzari, G. Experimental results on the retrofitting of hollow brick masonry walls with reinforced high performance mortar coatings. *Constr. Build. Mater.* **2017**, *141*, 619–630. [CrossRef]
5. Kouris, L. Alexandros, S.; Triantafillou, T.C. State-of-the-art on strengthening of masonry structures with textile reinforced mortar (TRM). *Constr. Build. Mater.* **2018**, *188*, 1221–1233. [CrossRef]
6. Gattesco, N.; Boem, I.; Dudine, A. Diagonal compression tests on masonry walls strengthened with a GFRP mesh reinforced mortar coating. *Bull. Earthq. Eng.* **2015**, *13*, 1703–1726. [CrossRef]
7. Angiolilli, M.; Gregori, A.; Pathirage, M.; Cusatis, G. Fiber Reinforced Cementitious Matrix (FRCM) for strengthening historical stone masonry structures: Experiments and computations. *Eng. Struct.* **2020**, *224*, 111102. [CrossRef]
8. Lucchini, S.S.; Facconi, L.; Minelli, F.; Plizzari, G. Retrofitting unreinforced masonry by steel fiber reinforced mortar coating: Uniaxial and diagonal compression tests. *Mater. Struct.* **2020**, *53*, 1–22. [CrossRef]
9. Sevil, T.; Baran, M.; Bilir, T.; Canbay, E. Use of steel fiber reinforced mortar for seismic strengthening. *Constr. Build. Mater.* **2011**, *25*, 892–899. [CrossRef]
10. Facconi, L.; Conforti, A.; Minelli, F.; Plizzari, G.A. Improving shear strength of unreinforced masonry walls by nano-reinforced fibrous mortar coating. *Mater. Struct.* **2015**, *48*, 2557–2574. [CrossRef]
11. Facconi, L.; Minelli, F.; Lucchini, S.; Plizzari, G. Experimental study of solid and hollow clay brick masonry walls retrofitted by steel fiber-reinforced mortar coating. *J. Earthq. Eng.* **2020**, *24*, 381–402. [CrossRef]
12. Di Nino, S.; D'Annibale, F.; Luongo, A. A simple model for damage analysis of a frame-masonry shear-wall system. *Int. J. Solids Struct.* **2017**, *129*, 119–134. [CrossRef]
13. Noor-E-Khuda, S.; Dhanasekar, M. Masonry walls under combined in-plane and out-of-plane loadings. *J. Struct. Eng.* **2018**, *144*, 04017186. [CrossRef]
14. Di Nino, S.; Zulli, D. Homogenization of ancient masonry buildings: A case study. *Appl. Sci.* **2020**, *10*, 6687. [CrossRef]

15. D'Altri, A.M.; Sarhosis, V.; Milani, G.; Rots, J.; Cattari, S.; Lagomarsino, S.; Sacco, E.; Tralli, A.; Castellazzi, G.; de Miranda, S. Modeling strategies for the computational analysis of unreinforced masonry structures: Review and classification. *Arch. Comput. Methods Eng.* **2020**, *27*, 1153–1185. [CrossRef]
16. Di Nino, S. Numerical investigations on infilled frames and predictive formulae in the elastic regime. *Eng. Struct.* **2022**, *250*, 113349. [CrossRef]
17. Pande, G.N.; Liang, J.X.; Middleton, J. Equivalent elastic moduli for brick masonry. *Comput. Geotech.* **1989**, *8*, 243–265. [CrossRef]
18. Cluni, F.; Gusella, V. Homogenization of non-periodic masonry structures. *Int. J. Solids Struct.* **2004**, *41*, 1911–1923. [CrossRef]
19. Lourenço, P.B.; Milani, G.; Tralli, A.; Zucchini, A. Analysis of masonry structures: Review of and recent trends in homogenization techniques. *Can. J. Civ. Eng.* **2007**, *34*, 1443–1457. [CrossRef]
20. Zucchini, A.; Lourenço, P.B. A micro-mechanical homogenisation model for masonry: Application to shear walls. *Int. J. Solids Struct.* **2009**, *46*, 871–886. [CrossRef]
21. Taliercio, A. Closed-form expressions for the macroscopic in-plane elastic and creep coefficients of brick masonry. *Int. J. Solids Struct.* **2014**, *51*, 2949–2963. [CrossRef]
22. Di Nino, S.; Luongo, A. A simple homogenized orthotropic model for in-plane analysis of regular masonry walls. *Int. J. Solids Struct.* **2019**, *167*, 156–169. [CrossRef]
23. Cecchi, A.; Milani, G.; Tralli, A. In-plane loaded CFRP reinforced masonry walls: Mechanical characteristics by homogenisation procedures. *Compos. Sci. Technol.* **2004**, *64*, 2097–2112. [CrossRef]
24. Milani, G. Kinematic FE limit analysis homogenization model for masonry walls reinforced with continuous FRP grids. *Int. J. Solids Struct.* **2011**, *48*, 326–345. [CrossRef]
25. Bertolesi, E.; Milani, G.; Poggi, C. Simple holonomic homogenization model for the non-linear static analysis of in-plane loaded masonry walls strengthened with FRCM composites. *Compos. Struct.* **2016**, *158*, 291–307. [CrossRef]
26. Zampieri, P.; Simoncello, N.; Libreros, J.G.; Pellegrino, C. Bond behavior of steel fiber-reinforced mortar (SFRM) applied onto masonry substrate. *Arch. Civ. Mech. Eng.* **2020**, *20*, 92. [CrossRef]
27. Buyukkaragoz, A.; Kopraman, Y. In-plane behaviour of masonry brick walls strengthened with mortar from two sides. In *Structures*; Elsevier: Amsterdam, The Netherlands, 2021; Volume 29, pp. 1627–1639.
28. Facconi, L.; Lucchini, S.S.; Minelli, F.; Plizzari, G.A. Analytical model for the in-plane resistance of masonry walls retrofitted with steel fiber reinforced mortar coating. *Eng. Struct.* **2023**, *275*, 115232. [CrossRef]
29. Lucchini, S.S.; Facconi, L.; Minelli, F.; Plizzari, G.A. Analytical prediction of the seismic resistance of masonry buildings retrofitted by Steel Fiber Reinforced Mortar coatings. *Procedia Struct. Integr.* **2023**, *44*, 2286–2293. [CrossRef]
30. Di Nino, S.; Luongo, A. Two-step homogenized elastic model for in-plane analysis of coated masonry walls. *Eur. J. -Mech.-A/Solids* **2023**, *102*, 105107. [CrossRef]
31. Lewinski, T.; Telega, J.J. *Plates, Laminates and Shells: Asymptotic Analysis and Homogenization*; World Scientific: London, UK, 2000; Volume 52.
32. Pagano, N.J. Free edge stress fields in composite laminates. *Int. J. Solids Struct.* **1978**, *14*, 401–406. [CrossRef]

Disclaimer/Publisher's Note: The statements, opinions and data contained in all publications are solely those of the individual author(s) and contributor(s) and not of MDPI and/or the editor(s). MDPI and/or the editor(s) disclaim responsibility for any injury to people or property resulting from any ideas, methods, instructions or products referred to in the content.